A Comparison of ECM-based State-of-Charge Estimators for Lithium-Ion Batteries

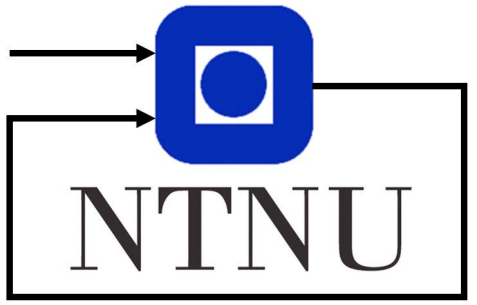

Author:
Daniel Dreyer Svendsen

Supervisor:
Damiano Varagnolo

Co-supervisor:
Walter Caharija

Specialization project
Department of Engineering Cybernetics
Norwegian University of Science and Technology

December 19, 2022

Preface

This report marks the end of the fall semester of my fifth year at the M.Sc. Cybernetics and Robotics study programme at NTNU. The work herein have been conducted in collaboration and consultation with Siemens Energy, and is considered a preliminary project before the main project in the master thesis. Hopefully the continued collaboration and work will be just as interesting as this one.

Acknowledgements

I would like to extend my gratitude and appreciation to my supervisor Professor Damiano Varagnolo at NTNU and my co-supervisor Walter Caharija and battery expert Daniel Grübl at Siemens Energy for their help, guidance and encouraging words throughout this fall semester. The completion of this specialization project would not have been possible without them.

Executive summary

This thesis have evaluated and compared the performance of five different equivalent-circuit model (ECM) based state estimators for estimation of the state of charge (SOC) of a lithium-ion battery (LIB) cell. The utilized state estimators were the Luenberger observer, the linear Kalman filter, the linear Moving Horizon Estimator, the extended Kalman filter and the Sigma-Point Kalman filter. All estimators achieved a RMS error below 3 $\%$ in the simulations that were run. The best performing estimator was the Sigma-Point Kalman filter (SPKF), with RMS estimation error below 1 $\%$ at a relatively low computational cost. The SPKF should therefore be investigated more closely in further work. Moreover, the potential performance of the Moving Horizon Estimator (MHE) as indicated by literature suggest that it is worth looking deeper into for nonlinear models.

Table of Contents

List of Tables

List of Figures

Abbreviations

Abbreviation	Description
LIB	Lithium-Ion Battery
EV	Electric Vehicle
BMS	Battery Management System
SOC	State of Charge
SOH	State of Health
SOAP	State of Available Power
ECM	Equivalent-Circuit Model
OCV	Open-Circuit Voltage
RC	Resistor-Capacitor
SPM	Single Particle Model
LKF	Linear Kalman Filter
MHE	Moving Horizon Estimator
EKF	Extended Kalman Filter
SPKF	Sigma-Point Kalman Filter
MHE	Moving Horizon Estimator
PCM	Parallel Cell Module
SCM	Series Cell Module

1

Introduction

1.1 Background

Lithium-ion batteries (LIBs) are extensively used as an energy storage technology, and their usage and areas of application are growing. They provide high energy density, low weight, a long lifespan, and can be a vital component in the transition to energy sustainability [8]. They have proven to be a preferred power source in electric vehicles (EVs) such as electric cars and electric ships, where safety and integrity concerns are particularly important [9]. In such usage, a battery management system (BMS) is essential. The BMS monitor and control the condition of the batteries to optimize their operation, and more importantly to ensure safe operation.

Internal states such as state of charge (SOC), state of health (SOH) and state of available power (SOAP) in the LIB are essential to monitor and control to provide safe operation [10]. These quantities cannot be measured directly, and therefore a BMS must provide accurate estimates of the internal states in real-time. This is not a trivial task, as batteries are time-varying, nonlinear systems that are significantly affected by temperature and noise, and thus they become difficult to model accurately. The importance of accurate models cannot be understated if model-based estimation is to be used [11]. Methods that use no models are for instance the Coulomb counting method, which measures and 'counts' the amount of charge that is going in and out of the battery. Model-based estimation is however more suitable for EV applications due to increased estimation accuracy and other advantages [12] [13]. The battery models can be divided into three categories, namely physics-based electrochemical models, equivalent-circuit models (ECMs) and data-driven models [11].

1.2 Problem description

The main goal of this thesis is to evaluate and compare the performance of five different ECM-based state estimators for state of charge estimation in lithium-ion batteries. These state estimators are namely the Luenberger observer, the linear Kalman filter (LKF), the Moving Horizon Estimator (MHE), the extended Kalman filter (EKF) and the Sigma-Point Kalman filter (SPKF). The Luenberger observer, the LKF and the MHE are evaluated with a linear LIB model, whereas the EKF and the SPKF are evaluated with a nonlinear model. The result of the comparison will lay the foundation and the set the course of further work to be conducted in a master thesis within state estimation for LIBs. Smaller additional problems and simulations are covered in the thesis as well. These include investigating the possibility of running battery pack simulations, EV simulations and using physics-based models in simulations.

1.3 Delimitations

The scope of the thesis has been narrowed down to SOC estimation for ECM-models in terms of the estimation problem. Hence SOH and SOAP estimation, as well as SOC estimation using physics-based models and data-driven models, are disregarded at this time. Note that there exists other defined internal states of LIBs, which are also not covered herein.

1.4 Structure of the report

The report is divided into eight chapters, where the current one is the first. Following the second chapter presents relevant theory needed in order to perform and understand state estimation of LIBs, before modeling of lithium-ion batteries are presented in chapter three. The state estimators that are utilized with these models are then presented in chapter four. Chapter five proceeds with laying forward the experimental methods that have been used during the work of this thesis, where the results that were obtained here are presented in chapter six. These results are then discussed and concluded upon in the two last chapters.

2

Theory

2.1 Lithium-ion Batteries

This section presents the basic working principle of rechargeable lithium-ion batteries relevant for this project thesis. In practice an LIB can be a single lithium-ion cell, or it may be constructed by two or more interconnected cells to increase the delivered power. One lithium-ion cell consists of four major elements: two electrodes: anode and cathode, a separator and electrolyte [14]. The typical setup is shown in Figure 2.1 with the corresponding chemical reaction equation.

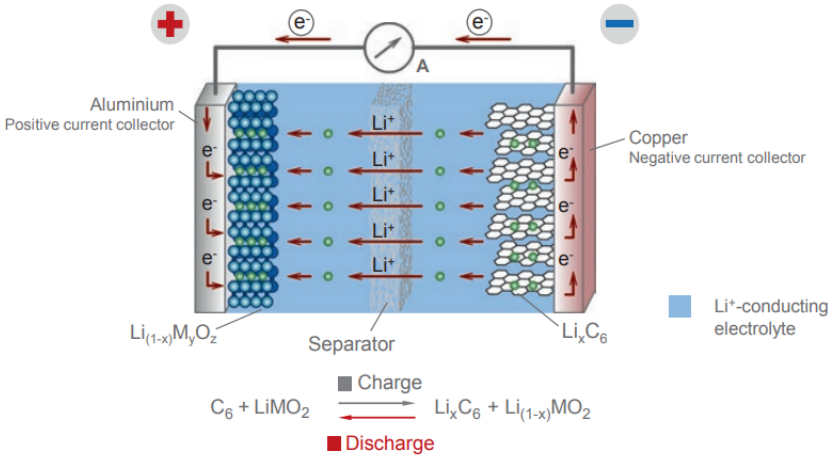

Figure 2.1: The setup of an LIB during a discharge process [1].

Here the anode consists of an active material in Li_xC_6 and a negative current collector of copper. The cathode have an active material of $Li_{(1-x)}M_yO_z$ and a positive current collector of aluminum. These electrodes are surrounded with lithium-ion conducting electrolyte, and are electrically isolated from each other by a separator. The separator allows for flow of lithium-ions between the electrodes, but not electrons. Thus by connecting the two electrodes together with an external conductive cable, a flow of electrons, or current, can occur [1].

During discharge, due to a difference in electrochemical potential energy between the electrodes creating an electromotive force, the favoured reaction is that the active material in the anode releases lithium-ions into the electrolyte, and electrons into the external circuit. The resulting flow of electrons can be utilized to do useful work, e.g. powering a device. During charging, the mentioned reaction is reversed [3].

2.2 Capacity C

To orderly define other relevant and important internal states of the battery later in the report, a clear definition of a battery's capacity C is needed. The actual capacity C of a battery is the amount of electric charge that a fully charged battery can deliver under predetermined reference conditions, and is given in unit of ampere-hours (Ah). The fully charged and empty state of the battery is defined by the manufacturer. Due to aging of the battery during its lifetime, the actual capacity will continuously decrease from the '*beginnng of life*' (BOL) until its '*end of life*' (EOL) [15].

2.3 State of charge

An LIB's state of charge (SOC) can be defined as the ratio between the available capacity and the total available capacity of a fully charged battery under reference conditions. In short:

$$SOC = SOC(t) = \frac{q(t)}{C} \tag{2.1}$$

where q(t) is the available capacity, or equivalently, the stored electric charge in the battery at a given point in time [15]. The SOC is a unitless number in the range $[0 \quad 1]$ or $[0\% \quad 100\%]$, where SOC = 100 % implies a fully charged battery and SOC = 0 % implies a fully discharged battery [3]. Throughout the report the SOC is denoted by the letter z.

2.4 Open-circuit voltage

The battery's open-circuit voltage (OCV) is the voltage between the terminals of the battery when there is no battery current. In general, since stored electric charge $q(t)$ is depen-

dent on time, and since the open-circuit voltage is dependent on the stored electric charge in the battery, then OCV(t) can also be seen as time dependent. Also, since the SOC is dependent on $q(t)$, the OCV can be described as dependent on the SOC of the battery [15]. The latter relationship will be used in this report, and it is often a static function that is found experimentally in laboratories under specific conditions, such as constant temperature for instance [3]. For further reading, this relationship is described by the function $OCV(z(t))$.

2.5 Polarization voltages

Polarization in lithium-ion batteries refers to the voltages that create a notable deviation in terminal voltage and open-circuit voltage due to a current flowing in the cell [3]. There are several different polarization phenomena present in an LIB during charge and discharge cycles, and they all have in common that they cause loss of energy and decreases the efficiency of the cell. Typical forms of polarization are ohmic polarization, activation polarization and concentration polarization. These occur in different parts of the cell, and their individual voltage contributions varies with the external cell excitation current [16]. In [17], the deviation is formulated as

$$V_{bat} - V_{OCV} = V_{ohmic} + V_{f,pos} + V_{f,neg} + V_{act,pos} + V_{act,neg} + V_{con} \tag{2.2}$$

where $V_{f,pos}$ and $V_{f,neg}$ represent the voltage drop due to passivation films or layers on the postive and negative electrodes, and $V_{f,act}$ and $V_{f,act}$ are voltage drops due to interfacial charge-transfer reactions at the electrodes. V_{con} adds the polarization obtained from phenomena such as lithium diffusion.

Ohmic polarization represents the general limitation in conductivity of ions and electrons in the current collectors, active materials, terminals, connectors and electrolyte [17]. This can be modeled through Ohm's law with a resistor R_0 to indicate the near instantaneous voltage drop that occurs when a battery current is passing through the cell, such that

$$V_{ohmic} = R_0 i_{bat} \tag{2.3}$$

where i_{bat} is the battery current [3].

Activation polarization occurs since the electrochemical reaction rate at the electrodes is lower than the electron velocity [18], This phenomena will not be elaborated or explored in any greater detail. Concentration polarization implies voltage drops due to effects such as diffusion, migration and convection [17]. Of relevance for this report is the diffusion dynamics.

2.6 Warburg impedance

For alternating current excitations of batteries, the electrochemical interface of the battery shows resistance in terms of impedance. This can be modeled and explained with an equivalent-circuit, namely the Randles circuit depicted in Figure 2.2.

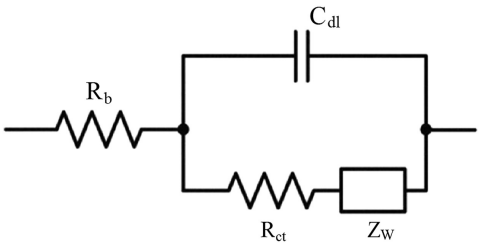

Figure 2.2: The Randles circuit [2].

The resistor R_b represents the bulk resistance of the cell, where the resistance in the electric conductivity in the electrolyte, separator and electrodes is considered. The resistor R_{ct} models the charge transfer resistance and the capacitor C_{dl} stands for the double layer capacitance. These two in combination contributes to the activation polarization. The Warburg impedance element Z_w models the impedance due to diffusion of lithium-ions in the cell [2], which is part of the concentration polarization. The Warburg impedance element may be described by

$$Z_w = \frac{A_w}{\sqrt{j\omega}} \tag{2.4}$$

where A_w is called the Warburg coefficient and frequency ω is given in $\frac{rad}{s}$. A Nyquist plot of the cell impedance is shown in Figure 2.3.

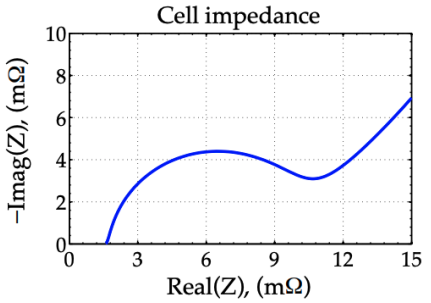

Figure 2.3: Nyquist plot of a realistic cell's electrochemical impedance spectrum (EIS) [3].

Here it can be observed that at low frequencies, a straight line of 45° appears in the EIS, which is due to the 45° phase shift that is contributed by the Warburg element to the cell.

For the intermediate frequencies, the charge transfer dynamics are represented, which are modeled by the RC pair. At the intersection between the curve and the real axis, the impedance in the cell in form of pure ohmic resistance R_b is found [3].

As there is no simple ordinary-differential equation for the dynamics of the Warburg impedance element, simulations using the Randle's circuit becomes cumbersome. In order to model and simulate these dynamics, the Warburg element can be approximated by multiple resistor-capacitor subcircuits in series, as illustrated in Figure 2.4.

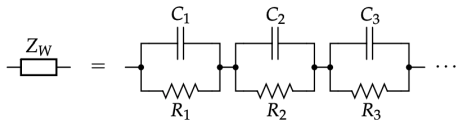

Figure 2.4: Approximation of the Warburg impedance element using RC subcircuits [3].

To be equivalent to the original Warburg element, an infinite number of RC subcircuits is required. However, over some frequency range, a reasonably small number of RC subcircuits can model the diffusion effects very well [3].

2.7 Hysteresis

The OCV is present in most equivalent-circuit models (ECMs), and the OCV as a function of the SOC is principal in many aspects when it comes Battery Management Systems. If the OCV-SOC relationship is well known, the SOC can be determined based on the OCV. However, this assumes a one-to-one relationship between the two, which is not the case if hysteresis is present [19]. In short, hysteresis in LIBs originates from entropic stress, mechanical stress and microscopic distortions within the active materials in the electrodes [20]. A consequence of this is that the cell relaxes to a different OCV depending on if the cell was last charging or discharging, which implies that there exists several possible open-circuit voltages for the the same SOC. This can cause signifacant inaccuracy in SOC estimation. To improve on this accuracy, some knowledge of the charge-discharge history must be included in the modeling [19]. However, it is in general difficult to model hysteresis because it is not a phenomena that is very well understood [3].

3

Modeling of battery cells

In this chapter two different approaches to modeling of battery cells are presented. The main focus, and the majority of the models that will be presented here, are equivalent-circuit models. The ECMs may be represented by circuit diagrams, as can be seen in the following sections, where the circuit dynamics is meant to approximate the behaviour of a battery cell with regards to how voltage responds to different input currents [3]. Moreover, one section will include a physics-based model that represent the electrochemical processes inside a battery on a micro-scale level, in order to demonstrate some of the most important dynamics that are present here. The equivalent-circuit method is thereby the first method of modeling, whereas physics-based methods is the second. For all the models the discrete-time equations will be given. This is because these models are intended for use in a discrete computer system in a BMS for real-time applications.

3.1 The Rint model

One of the simplest Equivalent-Circuit models is the *Rint model* [21] [3], which is represented by the circuit diagram shown in Figure 3.1. The ideal voltage source models the Open-Circuit voltage of the battery, which is a static function of the state of charge, $z(t)$. The resistor R_0 models the instantaneous internal ohmic resistance in the battery cell, and $i(t)$ is the load current defined as positive in its shown direction. This direction of load current implies a discharge of the battery cell.

The behaviour of this model in continuous time can be described by

$$\dot{z}(t) = -\eta(t)\frac{i(t)}{Q} \tag{3.1}$$

$$v(t) = OCV(z(t)) - R_0 i(t) \tag{3.2}$$

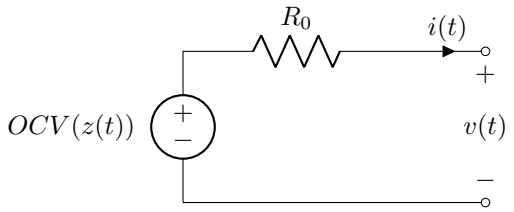

Figure 3.1: The Rint ECM.

or in discrete-time as

$$z_{k+1} = z_k - \frac{\Delta t}{Q}\eta_k i_k \tag{3.3}$$

$$v_k = OCV(z_k) - R_0 i_k \tag{3.4}$$

where $\eta(t)$ is the coloumbic efficiency and Q is the nominal capacity in units ampere-seconds As.

3.2 The Thevenin model

Another popular ECM is the *Thevenin model* [21][3], illustrated in the circuit diagram in Figure 3.2. The difference from the Rint model is that an RC subcircuit has been added, in order to model the slow diffusion process of lithium-ions in the battery cell. These voltages are referred to as *diffusion voltages*.

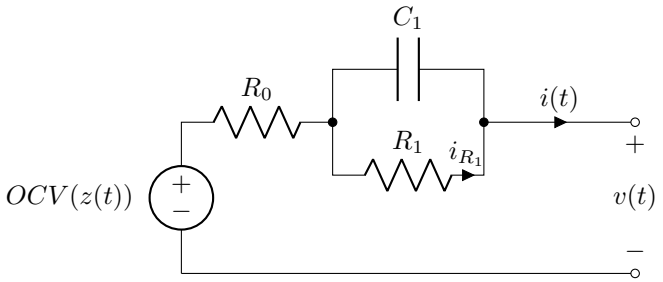

Figure 3.2: The Thevenin ECM.

The dynamics of the model may be described by

$$\dot{z}(t) = -\eta(t)\frac{i(t)}{Q} \tag{3.5}$$

$$\dot{i}_{R_1}(t) = -\frac{1}{R_1 C_1} i_{R_1}(t) + \frac{1}{R_1 C_1} i(t) \tag{3.6}$$

$$v(t) = OCV(z(t)) - R_1 i_{R_1}(t) - R_0 i(t) \tag{3.7}$$

or in discrete time

$$z_{k+1} = z_k - \frac{\Delta t}{Q}\eta_k i_k \tag{3.8}$$

$$i_{R_1,k+1} = \exp\left(\frac{\Delta t}{R_1 C_1}\right) i_{R_1,k} + \exp\left(1 - \frac{\Delta t}{R_1 C_1}\right) i_k \tag{3.9}$$

$$v_k = OCV(z_k) - R_1 i_{R_1,k} - R_0 i_k \tag{3.10}$$

3.3 The enhanced self-correcting model

A slightly more advanced ECM compared to the preceding models, namely the *enhanced self-correcting* (ESC) model [3], can be observed in Figure 3.3. In addition to the elements found in the previous models, the ESC model also contain a nonlinear *hysteresis* element to account for voltage hysteresis in the battery cell.

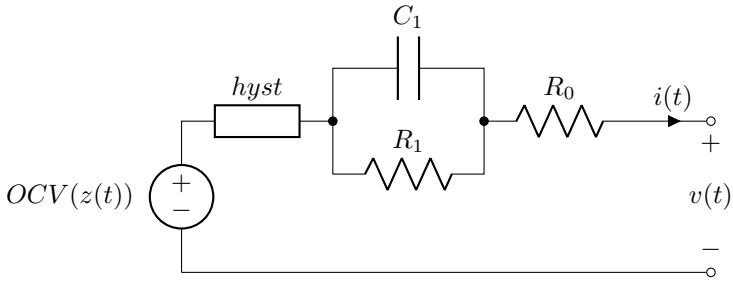

Figure 3.3: The enhanced self-correcting ECM.

Here a nonlinear time-varying system, as proposed in [3], is used to model hysteresis $h(t)$ somewhat simple. The differential equation of the element is given by

$$\dot{h}(t) = -\left|\frac{\eta(t) i(t) \gamma}{Q}\right| h(t) + \left|\frac{\eta(t) i(t) \gamma}{Q}\right| M(z, \dot{z}) \tag{3.11}$$

whereas in discrete-time the difference equation when using the simple representation $M(z, \dot{z}) = sgn(i_k)$ becomes

$$h_{k+1} = \exp\left(-\left|\frac{\eta_k i_k \gamma \Delta t}{Q}\right|\right) h_k + \left(\exp\left(-\left|\frac{\eta_k i_k \gamma \Delta t}{Q}\right|\right) - 1\right) sgn(i_k) \tag{3.12}$$

where in addition to the previously defined parameters, $\gamma > 0$ tunes the rate of decay for the hysteresis voltage. The state h_k accounts for dynamic hysteresis. By also adding a memory variable s_k, instantaneous hysteresis is accounted for. Let

$$s_k = \begin{cases} sgn(i_k), & |i_k| > 0 \\ s_{k-1} & \text{otherwise} \end{cases} \tag{3.13}$$

The full model is represented by

$$z_{k+1} = z_k - \frac{\Delta t}{Q}\eta_k i_k \tag{3.14}$$

$$i_{R_1,k+1} = \exp\left(\frac{\Delta t}{R_1 C_1}\right) i_{R_1,k} + \exp\left(1 - \frac{\Delta t}{R_1 C_1}\right) i_k \tag{3.15}$$

$$h_{k+1} = \exp\left(-\left|\frac{\eta_k i_k \gamma \Delta t}{Q}\right|\right) h_k + \left(\exp\left(-\left|\frac{\eta_k i_k \gamma \Delta t}{Q}\right|\right) - 1\right) sgn(i_k) \tag{3.16}$$

$$v_k = OCV(z_k) + Mh_k + M_0 s_k - R_1 i_{R_1,k} - R_0 i_k \tag{3.17}$$

3.4 The single particle model

The single particle model (SPM) is a physics-based electrochemical model that describes the dynamics inside a lithium-ion battery on a microscale level [3]. In general, the microscale models describes the chemical and physical processes that occur in the assumed homogeneous materials inside the battery. This includes the movement of particles in the solid material electrodes and in the electrolyte. Here a set of five coupled equations make up microscale cell models, which describes the following:

1. Charge conservation in the homogeneous solid electrode.
2. Mass conservation in the solid material electrode.
3. Mass conservation in the electrolyte.
4. Charge conservation in the homogeneous electrolyte.

However, the SPM only considers point 2, mass conservation in the homogeneous solid electrode active material. This is due to the fact that diffusion of lithium ions inside the solid active material in the electrodes in the cell is the slowest process, and therefore the dominant dynamics. Thus only the equations predicting this diffusion is used. The model can be considered relatively simple when compared to other physics-based models, but it provides a good basis for understanding the dynamics that are present at this level. Moreover it can be used to make good estimations of the state of charge for an LIB. In continuous-time, the lithium-ion diffusion equation reads as

$$\frac{\partial c_s}{\partial t} = \nabla \cdot (D_s \nabla c_s) \tag{3.18}$$

which in brief states that the rate of change of lithium concentration in every sample volume within the homogeneous solid electrode is equal to the total lithium flux density into that volume. Here c_s denotes the lithium concentration, $\nabla\cdot$ the divergence operator, ∇ the gradient operator and D_s is the diffusion coefficient. The subscript s implies that this is in solid phase [3].

The following presents a finite-volume method for discretizing the diffusion equation (3.18) [3]. A simplification made here is to consider an electrode as a spherical particle of the the relevant active material in the electrode. The spherical particle is divided into shells of equal thickness, similar to the shell-structure of an onion. Then each time step, the total flux of lithium from one shell to another is computed, and the concentration of lithium in each shell is updated. This flux is forced into or out of the particle through the outermost shell by an applied cell current. Assume the following:

- The particle has a radius R_s
- There are N_r shells of equal thickness, thus each shell has thickness $dR = R_s/N_r$.
- The innermost shell has volume $dV_1 = \frac{4}{3}\pi(dR)^3$ and an outer surface area $Sa_1 = 4\pi(dR)^2$
- The next shell has volume $dV_2 = \frac{4}{3}(2dR)^3 - dV_1$ and outer surface area $Sa_2 = 4\pi(2dR)^2$
- Following the same pattern yields the nth shell volume $dV_n = \frac{4}{3}\pi(ndR)^3 - \frac{4}{3}\pi((n-1)dR)^3$ and surface area $Sa_n = 4\pi(ndR)^2$

The molar flux density N as function of distance r is now discretized by

$$N = -D_s \nabla c_s = -D_s \frac{\partial c_s}{\partial r} \approx -D_s \frac{\Delta c_s}{\Delta r} \tag{3.19}$$

Thus the flux density each time step in or out from one shell to the next is stated as

$$N_n \approx -D_s \frac{c_{n+1} - c_n}{dR} \tag{3.20}$$

A negative N_n corresponds to flux entering the nth shell from the $(n+1)$st shell, and a positive N_n corresponds to flux leaving the nth shell to the $(n+1)$st shell. The unit of this flux density is given in $mol\ m^{-2}s^{-1}$. By multiplying each shell's flux at the shell boundaries with its surface area, the total rate of lithium movement is obtained in unit $mol\ s^{-1}$, i.e.

$$M_n = N_n Sa_n = -D_s \frac{c_{n+1} - c_n}{dR} Sa_n \tag{3.21}$$

Note that an exception for this is the outermost shell, which will be addressed shortly. The change in in lithium concentration for each of the $n-1$ inner shells per time step is then

$$\Delta c_{n,k} = \frac{N_n Sa_n - N_{n-1} Sa_{n-1}}{dV_n} \Delta t \tag{3.22}$$

At the outermost shell an applied flux density j is taken into account. Thus the change in concentration at the outermost shell is

$$\Delta c_{n,k} = j \frac{Sa_n \Delta t}{V_n} \tag{3.23}$$

where the applied flux density j is calculated by

$$j = \frac{i_{app}}{a_s FAL} mol\ m^{-2} s^{-1} \tag{3.24}$$

and i_{app} is the applied cell current in ampere A, $a_s = \frac{3\varepsilon_s}{R_s}$ where ε_s is the total surface area of electrode per volume of electrode in the cell. Moreover F is Faraday´s constant, $A\ [m^2]$ is the cell-current collector area and $L\ [m]$ is the electrode thickness.

Now state of charge is given by the average concentration of lithium in the electrode. The average concentration is calculated by the total amount of lithium in an electrode divided by the total volume of the solid active material in the electrode. For a fully charged battery the negative electrode has an amount of lithium that is at is maximum allowed limit while the positive electrode is at its minimum allowed limit. These are limits are respectively defined as

$$c^{neg}_{s,avg}/c^{neg}_{s,max} = x_{100\%}, \quad c^{pos}_{s,avg}/c^{pos}_{s,max} = y_{100\%} \tag{3.25}$$

For the opposite case, when the negative electrode contains the minimum allowed amount of lithium, and the positive electrode is at its maximum amount, the notation $x_{0\%}$ and $y_{0\%}$ is used. Hence overall cell state of charge z is

$$z = \frac{c^{neg}_{s,avg}/c^{neg}_{s,max} - x_{0\%}}{x_{100\%} - x_{0\%}} = \frac{c^{pos}_{s,avg}/c^{pos}_{s,max} - y_{0\%}}{y_{100\%} - y_{0\%}} \tag{3.26}$$

4

State estimation

4.1 A modified linear model

To more easily deploy the linear state estimators to be presented in this chapter, the linear Thevenin model in section 3.2 was modified. The new model includes the assumptions of Gaussian white process-noise $\mathbf{w}_k$ and measurement-noise $\mathbf{v}_k$, which captures the model uncertainty and measurement noise, respectively. Secondly, the output equation has to be slightly modified to arrive at the measurement equation $\mathbf{y}_k$. The modified model is given by

$$\begin{aligned} \mathbf{x}_{k+1} &= \mathbf{A}\mathbf{x}_k + \mathbf{B}\mathbf{u}_k + \mathbf{w}_k \\ \mathbf{y}_k &= \mathbf{C}\mathbf{x}_k + \mathbf{D}\mathbf{u}_k + \mathbf{v}_k \end{aligned} \tag{4.1}$$

where

$$\mathbf{x}_k = \begin{bmatrix} z_k \\ i_{R_1,k} \end{bmatrix}, \quad \mathbf{u}_k = i_k$$

$$\mathbf{A} = \begin{bmatrix} 1 & 0 \\ 0 & \exp\left(\frac{\Delta t}{R_1 C_1}\right) \end{bmatrix}, \quad \mathbf{B} = \begin{bmatrix} -\frac{\Delta t}{Q} \\ \exp\left(1 - \frac{\Delta t}{R_1 C_1}\right) \end{bmatrix}$$

is unchanged. In order to produce a linear measurement equation $\mathbf{y}_k$, a given OCV-curve of the relevant cell can be approximated by the linear function

$$OCV(z_k) \approx az_k + b \tag{4.2}$$

such that the original output equation

$$v_k = OCV(z_k) - R_1 i_{R_1,k} - R_0 i_k \tag{4.3}$$

is approximated as

$$\hat{v}_k = (az_k + b) - R_1 i_{R_1,k} - R_0 i_k \tag{4.4}$$

implying that

$$\mathbf{y}_k = \hat{v}_k - b, \quad \mathbf{C} = \begin{bmatrix} a & -R_1 \end{bmatrix}, \quad \mathbf{D} = -R_0$$

Note that this approximation can be particularly inaccurate for $z_k < 10\,\%$, which is evident from Figure 4.1.

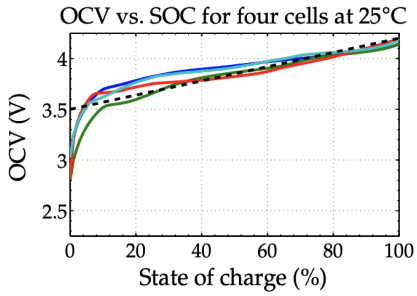

Figure 4.1: An example of a linear approximation of the OCV-SOC-relationship [4].

4.2 Luenberger observer

A widely used state estimator is the Luenberger observer. This observer uses a deterministic linear model to predict the model dynamics, where the predictions are corrected at each time step by feeding back output error in a closed loop [22]. The block diagram setup of the Luenberger observer is shown in Figure 4.2. For the Luenberger oberver, the model (4.5) is here used without the inclusion of process-noise $\mathbf{w}_k$ and measurement-noise $\mathbf{v}_k$ is used, i.e.

$$\begin{aligned} \mathbf{x}_{k+1} &= \mathbf{A}\mathbf{x}_k + \mathbf{B}\mathbf{u}_k \\ \mathbf{y}_k &= \mathbf{C}\mathbf{x}_k + \mathbf{D}\mathbf{u}_k \end{aligned} \tag{4.5}$$

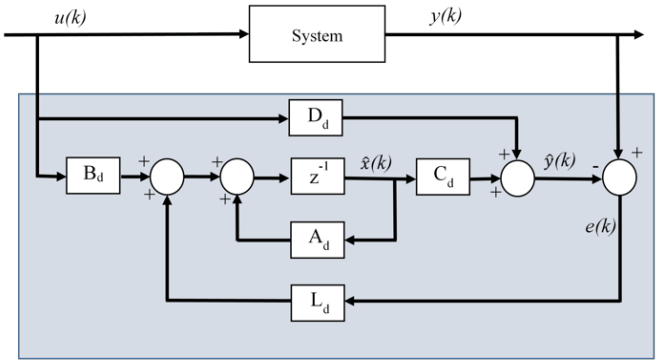

Figure 4.2: A block diagram of the Luenberger observer [5].

The observer provides an estimate $\hat{\mathbf{x}}_k$ of the system states at time step k according to the update law

$$\begin{aligned} \hat{\mathbf{x}}_{k+1} &= \mathbf{A}\hat{\mathbf{x}}_k + \mathbf{B}\mathbf{u}_k + \mathbf{L}(\mathbf{y}_k - \hat{\mathbf{y}}_k) \\ \hat{\mathbf{y}}_k &= \mathbf{C}\hat{\mathbf{x}}_k + \mathbf{D}\mathbf{u}_k \end{aligned} \tag{4.6}$$

where $\mathbf{y}_k$ is the actual measurement, $\hat{\mathbf{y}}_k$ is the estimated output and the differene between the two is the output error. The matrix $\mathbf{L}$ is the observer feedback gain, which is designed by pole placement. In the discrete time domain, this involves placing the eigenvalues of the matrix $(\mathbf{A} - \mathbf{LC})$ arbitrarily inside the unit circle in the complex plane to ensure a state estimation error $\mathbf{e} = \mathbf{x} - \hat{\mathbf{x}}$ that converges towards zero. Note that for this statement to hold, the pair $(\mathbf{A}, \mathbf{C})$ must be observable [23]. The process of pole placement is not a straight forward task, and the problem is dual to the task of pole placement for state feedback controllers. Generally poles placed closer to the origin yield a fast response of the observer, whereas poles placed closer to the edge of the unit circle yield a slower response. The former placement results in a observer that is a lot more to prone to amplification of noise, and the latter tends to attenuate noisy measurements [24].

4.3 Linear Kalman filter

Another popular state estimation algorithm is the linear Kalman filter (LKF). The LKF is a linear quadratic estimator that realizes the optimal solution to the Bayesian filter, under the assumptions of Guassian distributed uncertainties. The algorithm solves this probabilistic sequential inference problem in a recursive manner. The linear Kalman filter recursive algorithm is summarized below [4].

Algorithm 1 The linear Kalman filter

Linear state-space model:

$$\mathbf{x}_k = \mathbf{A}\mathbf{x}_{k-1} + \mathbf{B}\mathbf{u}_{k-1} + \mathbf{w}_{k-1}$$
$$\mathbf{y}_k = \mathbf{C}\mathbf{x}_k + \mathbf{D}\mathbf{u}_k + \mathbf{v}_k$$

Initialize: For k = 0

$$\hat{\mathbf{x}}_0^+ = \mathbb{E}[\mathbf{x}_0]$$
$$\mathbf{\Sigma}_{\tilde{\mathbf{x}},0}^+ = \mathbb{E}[(\mathbf{x}_0 - \hat{\mathbf{x}}_0^+)(\mathbf{x}_0 - \hat{\mathbf{x}}_0^+)^T]$$

Computation: For k = 1,2, ... end calculate:

Prediction part

A priori estimate: $\hat{\mathbf{x}}_k^- = \mathbf{A}\hat{\mathbf{x}}_{k-1}^+ + \mathbf{B}\mathbf{u}_{k-1}$

A priori state error-covariance matrix: $\mathbf{\Sigma}_{\tilde{\mathbf{x}},k}^- = \mathbf{A}\mathbf{\Sigma}_{\tilde{\mathbf{x}},k-1}^+\mathbf{A}^T + \mathbf{\Sigma}_{\bar{\mathbf{w}}}$

Output estimate: $\hat{\mathbf{y}}_k = \mathbf{C}\hat{\mathbf{x}}_k^- + \mathbf{D}\mathbf{u}_k$

Correction part

Kalman gain matrix: $\mathbf{L}_k = \mathbf{\Sigma}_{\tilde{\mathbf{x}},k}^-\mathbf{C}_k^T[\underbrace{\mathbf{C}_k\mathbf{\Sigma}_{\tilde{\mathbf{x}},k}^-\mathbf{C}_k^T + \mathbf{\Sigma}_{\bar{\mathbf{v}}}}_{\mathbf{\Sigma}_{\tilde{\mathbf{y}},k}}]^{-1}$

A posteriori estimate: $\hat{\mathbf{x}}_k^+ = \mathbf{A}\hat{\mathbf{x}}_k^- + \mathbf{L}_k(\mathbf{y}_k - \hat{\mathbf{y}}_k)$

A posteriori state error-covariance matrix: $\mathbf{\Sigma}_{\tilde{\mathbf{x}},k}^+ = \Sigma_{\tilde{\mathbf{x}},k}^- - \mathbf{L}_k\mathbf{\Sigma}_{\tilde{\mathbf{y}},k}\mathbf{L}_k^T$

4.4 Moving Horizon Estimator

The Moving Horizon Estimator (MHE) is a powerful state estimator that has obtained increasing success over the recent years. The MHE takes into consideration a series of noisy measurements over a fixed horizon N backwards in time, and solves an optimization problem that yields an optimal state estimate each time step k. The optimization problem can be formulated as a linear, quadratic or nonlinear program with constraints, implying that the MHE is able to handle both linear and nonlinear systems as well as system constraints during state estimation. Obtaining the solution of the optimization problem requires the use of a mathematical programming solver each iteration, which can be be a computationally expensive task [25].

Typically the optimization problem is formulated as a minimization of a cost function,

which in the literature come in different variants for the SOC estimation problem. Using the model (4.5), one such formulation based on [26] and [27] is

$$\begin{aligned}
\min_{\hat{\mathbf{x}}} \ & \|\hat{\mathbf{x}}_{k-N+1} - \bar{\mathbf{x}}_{k-N+1}\|^2_{P^{-1}_{k-N+1}} + \sum_{i=k-N+1}^{k} \|y_i - \mathbf{C}\hat{\mathbf{x}}_i - \mathbf{D}\mathbf{u}_i\|^2_{R^{-1}} \\
& + \sum_{i=k-N+1}^{k-1} ||\hat{\mathbf{x}}_{i+1} - \mathbf{A}\hat{\mathbf{x}}_i - \mathbf{B}\mathbf{u}_i||^2_{Q^{-1}} \\
& s.t. \\
& \bar{\mathbf{x}}_{k-N} \quad \text{given} \\
& y_{k-N+i} \quad \text{given}; \quad i = 1, ..., N \\
& u_{k-N+i} \quad \text{given}; \quad i = 1, ..., N \\
& \hat{\mathbf{x}}_{k-N+i+1} = \mathbf{A}\hat{\mathbf{x}}_{k-N+i} + \mathbf{B}\mathbf{u}_{k-N+i}; \quad i = 0, ..., N-1 \\
& 0 < \hat{z}_k < 1
\end{aligned} \tag{4.7}$$

Here $\mathbf{y}$ and $\mathbf{u}$ are sets of the N last voltage and current measurements respectively, and the solution $\hat{\mathbf{x}}$ is the optimal state estimates over the horizon N. Thus the optimal state estimate at time step k is the last element in the solution, denoted $\hat{\mathbf{x}}_k$. The intuition behind the formulation above is that one wants to minimize the deviation between measured and estimated output in the second term in the cost function, while also minimizing the deviation between the optimized state estimate and the propagated system dynamics in the third term. The desired penalization of these deviations are set by the constant weighting matrices $\mathbf{R}^{-1}$ and $\mathbf{Q}^{-1}$, which is set to be the inverse of the covariance matrices $\mathbf{R}$ and $\mathbf{Q}$ for the measurement and process noise respectively, as in [27] and [28].

The first term in the cost function is the *arrival cost*. This cost is an approximation that takes into account the information received up until $i = k - N + 1$, i.e. prior to the start of the current estimation horizon. Here the deviation between the initial estimate $\hat{\mathbf{x}}_{k-N+1}$ in the current horizon and the a priori estimate $\bar{\mathbf{x}}_{k-N+1}$ is penalized with the inverse covariance matrix $\mathbf{P}^{-1}_{\mathbf{k-N+1}}$ of the a priori estimate. The a priori estimate in the current horizon is the optimal estimate computed at $k - N + 1$ time steps back. Using this approximation of arrival cost is termed the filtering formulation of the MHE. In practice this can be implemented by running Kalman filter covariance matrix updates in parallel with the operation of the MHE, and then store the covariances for use N time steps later [28].

In [27], it is shown that if no constraints are active, the MHE and the Kalman filter are the same for linear systems. This is because the arrival cost approximation mentioned above becomes exact. There exist other MHE formulations, such as the *smoothing* formulation, which approximates the arrival cost slightly differently. This will however not be investigated in this thesis.

4.5 Extended Kalman filter

The linear Kalman filter that was presented in section 4.3 is only applicable to linear systems. In this section the *extended Kalman filter* (EKF) is implemented, which applies to nonlinear systems. Therefore, the EKF is here realized in combination with the nonlinear ESC model in (3.3) with additive Gaussian distributed measurement noise $\mathbf{v}_k$ and process noise $\mathbf{w_k}$. The general form of the nonlinear ESC model can be stated as

$$\begin{aligned} \mathbf{x}_{k+1} &= \mathbf{f}(\mathbf{x}_k, \mathbf{u}_k, \mathbf{w}_k) \\ \mathbf{y}_k &= \mathbf{g}(\mathbf{x}_k, \mathbf{u}_k, \mathbf{v}_k) \end{aligned} \tag{4.8}$$

The working principle of the EKF is similar to that of the LKF in terms of the prediction and correction steps, but due to the nonlinearites of the system, a linearization is performed each time step. The EKF makes two simplifying assumptions in order to apply the sequential probabilistic inference equations to a nonlinear model. Firstly, the approximation $\mathbb{E}[\mathbf{f}(\mathbf{x})] \approx \mathbf{f}(\mathbb{E}[\mathbf{x}])$ is used, which essentially states that the expected value of a nonlinear function $\mathbf{f}$ evaluated at the unknown state $\mathbf{x}$ is approximately the same as the nonlinear function $\mathbf{f}$ evalutated in the expected value of the unknown state $\mathbf{x}$. This is strictly exact only for linear systems, and therefore the approximation becomes worse the more nonlinear the function $\mathbf{f}$ is. Secondly, when computing the covariance matrices, EKF only uses a first-order Taylor series expansion when linearizing the system around the current operating point, and truncates the higher order terms. This also a reason that the EKF performs better for systems with mild nonlinearities. The EKF algorithm based on [29] and [4] used here is summarized below.

Algorithm 2 The extended Kalman filter

Nonlinear state-space model:

$$\mathbf{x}_k = \mathbf{f}(\mathbf{x}_{k-1}, \mathbf{u}_{k-1}, \mathbf{w}_{k-1})$$
$$\mathbf{y}_k = \mathbf{g}(\mathbf{x}_k, \mathbf{u}_k, \mathbf{v}_k)$$

where $\mathbf{w}_k$ are $\mathbf{v}_k$ are independent samples from Gaussian distributions with means $\bar{w}$ and $\bar{v}$ and covariance matrices $\mathbf{\Sigma}_{\bar{\mathbf{w}}}$ and $\mathbf{\Sigma}_{\bar{\mathbf{v}}}$.

Define linearization:

$$\hat{\mathbf{A}}_k = \left.\frac{\partial \mathbf{f}(\mathbf{x}_k, \mathbf{u}_k, \mathbf{w}_k)}{\partial \mathbf{x}_k}\right|_{\mathbf{x}_k = \hat{\mathbf{x}}_k^+} \quad , \quad \hat{\mathbf{B}}_k = \left.\frac{\partial \mathbf{f}(\mathbf{x}_k, \mathbf{u}_k, \mathbf{w}_k)}{\partial \mathbf{w}_k}\right|_{\mathbf{w}_k = \bar{\mathbf{w}}_k}$$
$$\hat{\mathbf{C}}_k = \left.\frac{\partial \mathbf{g}(\mathbf{x}_k, \mathbf{u}_k, \mathbf{v}_k)}{\partial \mathbf{x}_k}\right|_{\mathbf{x}_k = \hat{\mathbf{x}}_k^-} \quad , \quad \hat{\mathbf{D}}_k = \left.\frac{\partial \mathbf{g}(\mathbf{x}_k, \mathbf{u}_k, \mathbf{v}_k)}{\partial \mathbf{v}_k}\right|_{\mathbf{v}_k = \bar{\mathbf{v}}_k}$$

Initialize: For k = 0

$$\hat{\mathbf{x}}_0^+ = \mathbb{E}[\mathbf{x}_0]$$
$$\mathbf{\Sigma}_{\tilde{\mathbf{x}},0}^+ = \mathbb{E}[(\mathbf{x}_0 - \hat{\mathbf{x}}_0^+)(\mathbf{x}_0 - \hat{\mathbf{x}}_0^+)^T]$$

Computation: For k = 1,2, ... end, calculate:

Prediction part

A priori estimate: $\hat{\mathbf{x}}_k^- = \mathbf{f}(\hat{\mathbf{x}}_{k-1}^+, \mathbf{u}_{k-1}, \bar{\mathbf{w}}_{k-1})$

A priori state error-covariance matrix: $\mathbf{\Sigma}_{\tilde{\mathbf{x}},k}^- = \hat{\mathbf{A}}_{k-1}\mathbf{\Sigma}_{\tilde{\mathbf{x}},k-1}^+\hat{\mathbf{A}}_{k-1}^T + \hat{\mathbf{B}}_{k-1}\mathbf{\Sigma}_{\bar{\mathbf{w}}}\hat{\mathbf{B}}_{k-1}^T$

Output estimate: $\hat{\mathbf{y}}_k^- = \mathbf{g}(\hat{\mathbf{x}}_k^-, \mathbf{u}_k, \bar{\mathbf{v}}_k)$

Correction part

Kalman gain matrix: $\mathbf{L}_k = \mathbf{\Sigma}_{\tilde{\mathbf{x}},k}^-\hat{\mathbf{C}}_k^T[\underbrace{\hat{\mathbf{C}}_k\mathbf{\Sigma}_{\tilde{\mathbf{x}},k}^-\hat{\mathbf{C}}_k^T + \hat{\mathbf{D}}_k\mathbf{\Sigma}_{\bar{\mathbf{v}}}\hat{\mathbf{D}}_k^T}_{\approx\mathbf{\Sigma}_{\tilde{\mathbf{y}},k}}]^{-1}$

A posteriori estimate: $\hat{\mathbf{x}}_k^+ = \mathbf{A}\hat{\mathbf{x}}_k^- + \mathbf{L}_k(\mathbf{y}_k - \hat{\mathbf{y}}_k)$

A posteriori state error-covariance matrix: $\mathbf{\Sigma}_{\tilde{\mathbf{x}},k}^+ = \Sigma_{\tilde{\mathbf{x}},k}^- - \mathbf{L}_k\mathbf{\Sigma}_{\tilde{\mathbf{y}},k}\mathbf{L}_k^T$

4.6 Sigma-Point Kalman filter

The simplifying assumptions in the EKF causes reduced estimation accuracy for highly nonlinear systems, which merits the use of the Sigma-Point Kalman filter (SPKF) [30]. The SPKF substitutes local linearization with evaluation of the statistical distribution of the nonlinear system output by deterministic sampling [22]. More specifically the SPKF estimates the mean and variance of the outputs of a nonlinear function using a small, fixed set of function evaluations called *sigma-points*. For this purpose, a set of input sigma-points are carefully chosen such that the mean and covariance of the input points coincide with the mean $\bar{\mathbf{x}}$ and the covariance $\mathbf{\Sigma}_{\bar{\mathbf{x}}}$ of the random variable that is normally used as input to the nonlinear function. The input sigma-points are then propagated through the nonlinear function individually, yielding a transformed set of output sigma-points [4]. This transformation of sigma-points is referred to as the *unscented* transform [6]. In Figure 4.3 the difference between the actual sampling of the mean and variance of a transformed random variable $\mathbf{x}$ is shown and compared to that of the EKF and SPKF transformations. Notice how accurate the SPKF transformation is compared to the EKF transformation.

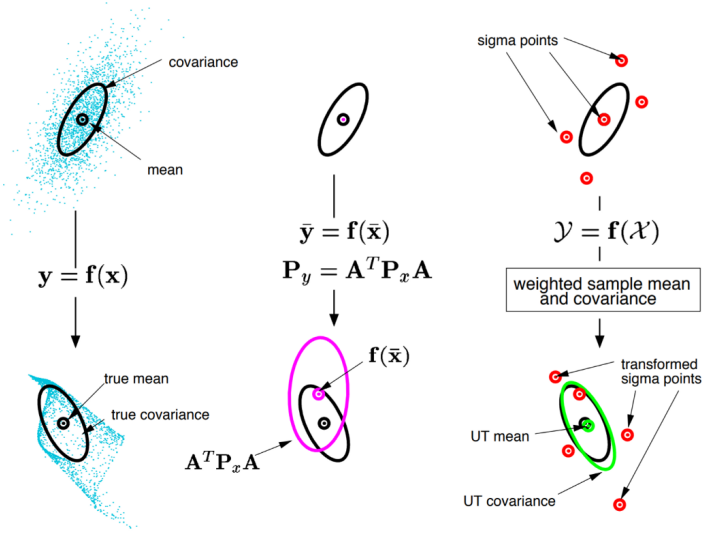

Figure 4.3: Illustration of the difference between actual sampling, linearized EKF transformation and the SPKF uscented transformation, in that order [6].

For details of how the different steps in the algorithm is derived, consult [4] for a comprehensive deduction. For the purpose of reasonable simplicity, a summary based on the same reference is provided below.

Algorithm 3 The Sigma-Point Kalman filter

Nonlinear state-space model:

$$\mathbf{x}_k = \mathbf{f}(\mathbf{x}_{k-1}, \mathbf{u}_{k-1}, \mathbf{w}_{k-1})$$
$$\mathbf{y}_k = \mathbf{g}(\mathbf{x}_k, \mathbf{u}_k, \mathbf{v}_k)$$

where $\mathbf{w}_k$ are $\mathbf{v}_k$ are independent samples from Gaussian distributions with means $\bar{w}$ and $\bar{v}$ and covariance matrices $\mathbf{\Sigma}_{\bar{\mathbf{w}}}$ and $\mathbf{\Sigma}_{\bar{\mathbf{v}}}$.

Define:

$$\mathbf{x}_k^a = [\mathbf{x}_k^T, \mathbf{w}_k^T, \mathbf{v}_k^T]^T, \quad \mathcal{X}_k^a = [(\mathcal{X}_k^x)^T,\ (\mathcal{X}_k^w)^T,\ (\mathcal{X}_k^v)^T]^T \ \text{(sigma-points)}$$
$$p = 2 \times \dim(\mathbf{x}_k^a)$$

Initialize: For k = 0

$$\hat{\mathbf{x}}_0^+ = \mathbb{E}[\mathbf{x}_0], \quad \mathbf{\Sigma}_{\tilde{\mathbf{x}},0}^+ = \mathbb{E}[(\mathbf{x}_0 - \hat{\mathbf{x}}_0^+)(\mathbf{x}_0 - \hat{\mathbf{x}}_0^+)^T]$$
$$\hat{\mathbf{x}}_0^{a,+} = \mathbb{E}[\mathbf{x}_0^a] = [(\hat{\mathbf{x}}_0^+)^T, \bar{\mathbf{w}}, \bar{\mathbf{v}}]^T$$
$$\mathbf{\Sigma}_{\tilde{\mathbf{x}},0}^{a,+} = \mathbb{E}[(\mathbf{x}_0^a - \hat{\mathbf{x}}_0^{a,+})(\mathbf{x}_0^a - \hat{\mathbf{x}}_0^{a,+})^T] = \mathit{diag}(\mathbf{\Sigma}_{\tilde{\mathbf{x}},0}^+, \mathbf{\Sigma}_{\tilde{\mathbf{w}}}, \mathbf{\Sigma}_{\tilde{\mathbf{v}}})$$

Computation: For k = 1,2, ... end, calculate:

Prediction part

A priori estimate:

$$\mathcal{X}_{k-1}^{a,+} = \left\{ \hat{\mathbf{x}}_{k-1}^{a,+}, \quad \hat{\mathbf{x}}_{k-1}^{a,+} + \gamma\sqrt{\Sigma_{\hat{x},k-1}^{a,+}}, \quad \hat{\mathbf{x}}_{k-1}^{a,+} - \gamma\sqrt{\Sigma_{\tilde{x},k-1}^{a,+}} \right\}$$
$$\mathcal{X}_{k,i}^{x,-} = \boldsymbol{f}\left(\mathcal{X}_{k-1,i'}^{x,+}, \mathbf{u}_{k-1}, \mathcal{X}_{k-1,i}^{w,+}\right)$$
$$\hat{\boldsymbol{x}}_k^- = \sum_{i=0}^{p} \alpha_i^{(\mathrm{m})} \mathcal{X}_{k,i}^{x,-}$$

A priori state error-covariance matrix:

$$\widetilde{\mathcal{X}}_{k,i}^{x,-} = \mathcal{X}_{k,i}^{x,-} - \hat{\mathbf{x}}_k^-$$
$$\mathbf{\Sigma}_{\tilde{\boldsymbol{x}},k}^- = \sum_{i=0}^{p} \alpha_i^{(\mathrm{c})} \left(\widetilde{\mathcal{X}}_{k,i}^{x,-}\right)\left(\widetilde{\mathcal{X}}_{k,i}^{x,-}\right)^T$$

Output estimate:

$$\mathcal{Y}_{k,i} = \boldsymbol{h}\left(\mathcal{X}_{k,i}^{x,-}, \boldsymbol{u}_k, \mathcal{X}_{k-1,i}^{v,+}\right)$$
$$\hat{\boldsymbol{y}}_k = \sum_{i=0}^{p} \alpha_i^{(\mathrm{m})} \mathcal{Y}_{k,i}$$

Correction part

Kalman gain matrix:

$$\tilde{\mathcal{Y}}_{k,i} = \mathcal{Y}_{k,i} - \hat{\mathbf{y}}_k$$
$$\boldsymbol{\Sigma}_{\tilde{y},k} = \sum_{i=0}^{p} \alpha_i^{(\mathrm{c})} \left(\tilde{\mathcal{Y}}_{k,i}\right) \left(\tilde{\mathcal{Y}}_{k,i}\right)^T$$
$$\boldsymbol{\Sigma}_{\tilde{x}\tilde{x},k}^{-} = \sum_{i=0}^{p} \alpha_i^{(\mathrm{c})} \left(\tilde{\mathcal{X}}_{k,i}^{x,-}\right) \left(\tilde{\mathcal{Y}}_{k,i}\right)^T$$
$$\mathbf{L_k} = \boldsymbol{\Sigma}_{\tilde{x}\tilde{y},k}^{-} \boldsymbol{\Sigma}_{\tilde{y},k}^{-1}$$

A posteriori estimate:

$$\hat{\mathbf{x}}_k^{+} = \mathbf{A}\hat{\mathbf{x}}_k^{-} + \mathbf{L}_k(\mathbf{y}_k - \hat{\mathbf{y}}_k)$$

A posteriori state error-covariance matrix:

$$\boldsymbol{\Sigma}_{\tilde{\mathbf{x}},k}^{+} = \boldsymbol{\Sigma}_{\tilde{\mathbf{x}},k}^{-} - \mathbf{L}_k \boldsymbol{\Sigma}_{\tilde{\mathbf{y}},k} \mathbf{L}_k^T$$

5

Experimental methodology

5.1 An identified linear LIB model

For testing and simulation of the linear state estimators, a first order Thevenin cell model identified in [7] was used. The model is of a 18650 $LiNiMnCoO_2$/Graphite lithium-ion cell, with specifications given in Table 5.1.

Type	Nominal voltage	Nominal capacity	Upper/lower cut-off voltage	Max. current	Usage temperature
18650	3.6 V	2.0 Ah	2.5 V/4.2V	22 A (at 25 °C)	0-50 °C

Table 5.1: LIB cell specifications.

In the aforementioned paper, a dynamic stress test (DST) was performed on several samples of the relevant LIB cell for model parameter identification. The DST is designed by the US Advanced Battery Consortium (USABC), and it is a dynamic discharge simulation that can be scaled to meet the maximum performance specifications of a battery. It is as a dynamic load current profile that has both discharge and charge steps of different amplitudes, as can be seen in Figure 5.1. Furthermore, a low-current OCV-SOC relationship for the given cell was found experimentally. This OCV-curve was approximated to a linear function in order to fit the modified linear model derived in section 4.1 by using the function *polyfit* in MATLAB.

In [7] they used the least squares (LS) algorithm to arrive at the identified Thevenin model parameters in Table 5.2.

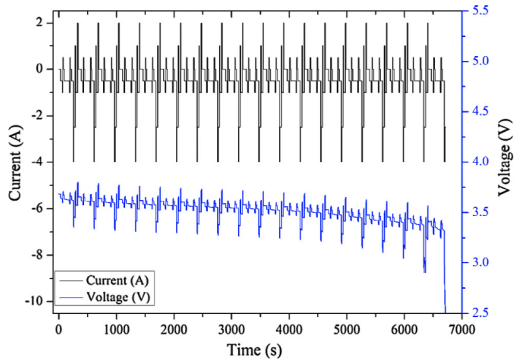

Figure 5.1: DST profile at 25 °C [7].

$R_0(\Omega)$	$R_1(\Omega)$	$C_1(F)$	RMS modelling error
0.0710	0.0222	1201.4	6.257e-4

Table 5.2: Identified Thevenin model paramters.

5.2 Test dataset

For performance evaluation of the linear state estimators with the identified linear model, the Federal Urban Driving Schedule (FUDS) was used. This load current profile has been, along with the DST profile in the last section, collected from the open dataset posted by the CALCE Battery Research Group online [7]. The FUDS is a more dynamic load current profile compared to the DST, and it is based on the cell-level current demand of a industry standard electric vehicle [31]. In particular, the FUDS associated with an ambient temperature of 25 °C, sampling time of $1s$ and an accurate inital SOC of 80% is used in the test simulations. In Figure 5.2 the FUDS current profile is shown.

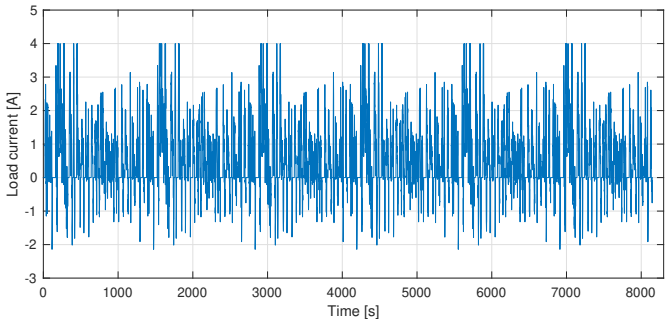

Figure 5.2: 6 cycles of the FUDS current profile.

5.3 Nonlinear estimation

The previous sections in this chapter have elaborated on methods of linear SOC estimation, which have been the main focus of this thesis. In order to get an introduction to nonlinear SOC estimation, a useful open source MATLAB toolbox and additional code handed out by Dr. Gregory L. Plett in [4] have been used. Here both the EKF and the SPKF have been simulated with use of the nonlinear ESC-model introduced in section 3.3. The toolbox contains six identified LIB cell models that fits the ESC-model and their corresponding OCV-SOC relationships for different temperatures ranging from - 25 °C to 45 °C. Moreover, empirical partial derivatives of the OCV-SOC curves have been provided, in order to readily simulate the EKF. In this thesis the E2 type cell with nonimal capacity of 5.16 Ah in the toolbox was used for performance evaluation of the nonlinear state estimators by applying 16 cycles of the provided Urban Dynamometer Driving Schedule (UDDS) load profile in Figure 5.3. The available specifications of the E2 type cell and the parameters of the corresponding indentified ESC-model are listed in Table 5.3.

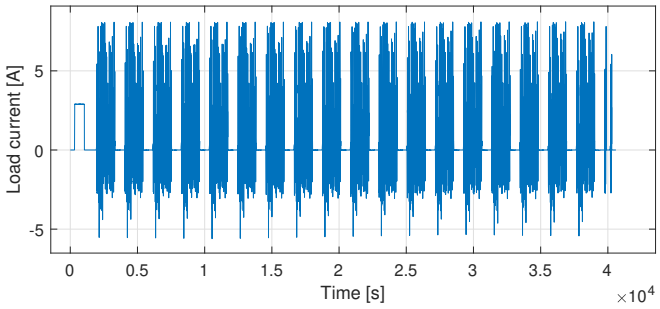

Figure 5.3: 16 cycles of the UDDS current profile.

$R_0(\Omega)$	$R_1(\Omega)$	$C_1(F)$	$M(V)$	$M_0(V)$	η	γ
0.0313	0.0071	256.6	0.0805	0	0.9776	106.2

Table 5.3: Available identified parameters for the ESC-model based on the E2 cell at an ambient temperature of 5 °C.

5.4 Single particle model simulation

Based on the equations for the physics-based single particle model in section 3.4, a simulation of the surface concentration of lithium in an electrode was performed. This was done purely to learn and observe the slow diffusion of lithium in an LIB, rather than employing this type of model for SOC estimation at this time. The simulation was performed with MATLAB code provided in the same reference in which the model itself was derived [3]. Simulation constants were defined as follows

- Spherical electrode particle radius: $R_s = 10^{-6}\ [m]$

- Maximum allowed concentration: $c_{max} = 12000\ [\frac{mol}{m^3}]$
- Initial lithium concentration: $c_0 = 9500\ [\frac{mol}{m^3}]$
- Initial lithium flux density: $j_0 = \frac{5000\frac{R_s}{3}}{1800}[\frac{mol}{m^2 s}]$

In the simulation the applied initial flux was held constant for 30 minutes, followed by no applied flux for 1 hour, followed by the negative of the initial flux for another 30 minutes, and at last no applied flux. Thus a discharge-rest-charge-rest lithium flux profile was applied.

5.5 Battery pack simulation

At a certain point the battery pack as a whole must be monitored and controlled in a BMS. A battery pack can consist of several interconnected cells that are assembled in modules, where the modules are interconnected to form packs [4]. In [4] parallel connected modules (PCM) and series connected modules (SCM) are mentioned. The PCM battery packs have parallel connected cells that are assembled in modules, where the modules are then connected together in series. The SCM battery packs are the opposite where the cells connected in series in each module, and then the modules are connected in parallel. Here the PCM configuration of a battery pack was simulated with MATLAB code provided in [4] to observe some of the minor variations in each individual module and cell that one in reality can expect. The cell model used here is also based on the E2 type cell in the ESC toolbox, with an ambient temperature of 25 °C.

For the PCM pack, total current and voltage is calculated by

$$i_k = \sum_{j=1}^{N_p} \frac{v_{fj,k}}{R_{0,j}} - v_k \sum_{j=1}^{N_p} \frac{1}{R_{0,j}} \tag{5.1}$$

$$v_k = \frac{\sum_{j=1}^{N_p} \frac{v_{fj,k}}{R_{0,j}} - i_k}{\sum_{j=1}^{N_p} \frac{1}{R_{0,j}}} \tag{5.2}$$

where $v_{fj,k}$ is the fixed voltage of cell j at timestep k, $R_{0,j}$ is the resistance of cell j and N_p is the number of modules. In the code random, small variations were added to each resistance $R_{0,j}$, the initial SOC of each cell and the total capacity of each cell to simulate the fact that no cell is exactly identical. The random SOC was placed in the range 30% - 70%, the random resistance in the range 5mΩ - 25mΩ and the random capacity in the range 4.5 Ah - 5.5 Ah. The load current was set to 10C, which is unrealistically high, but it serves to demonstrate some important aspects. 1C is the relative measure of current that explains how much constant current is needed to completely discharge the battery in 1 hour [3].

5.6 EV simulation

For electric vehicle (EV) applications it is essential to simulate the dynamics of the vehicle and asses the demanded performance from the battery pack before design and implementation of the battery pack. In [4] a comprehensive collection of MATLAB code for running EV simulations are given, and this was used here to perform EV simulations with the mentioned UDDS cycle. The simulation strategy is shown in Figure 5.4.

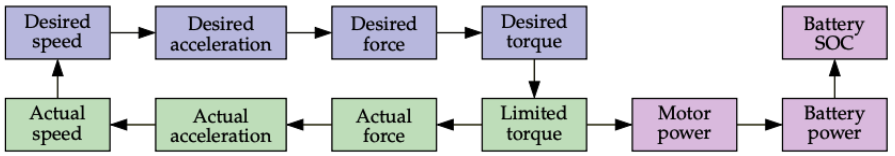

Figure 5.4: Simulation strategy of EV [4].

The simulation yields the desired and actual speed and acceleration of the EV during one UDDS cycle, and the corresponding battery power, current and SOC.

5.7 State estimator implementation

5.7.1 Luenberger observer, KF and MHE

The linear state estimators were all implemented and simulated in MATLAB using their respective algorithms and the identified Thevenin model. The Luenberger observer and the KF was implemented straight forward in a MATLAB script, whereas the MHE was implemented using the CasADi optimization toolbox in MATLAB [32]. The utilized solver here was the nonlinear 'IPOPT' solver in the toolbox.

For the Luenberger observer, the final tuning of the gain matrix L was obtained from the pole placement $p = [0.99, 0.98]$. For the KF and the MHE, two different tunings were implemented and tested. First, the covariance matrices ($\mathbf{\Sigma}_{\tilde{\mathbf{w}}}$ and $\mathbf{\Sigma}_{\tilde{\mathbf{v}}}$ for the KF, $\mathbf{Q}$ and $\mathbf{R}$ for the MHE) were set to be same as the covariance of the simulated white Gaussian process and measurement noise, which is often a good initial guess in practice. Thereafter the process noise covariance matrix of the two was reduced by a factor of 100, implying that the model should be trusted more than the measurements, to see if better results could be obtained.

Assuming that the process noise is current sensor noise and the measurement noise is voltage sensor noise, the applied random, white process noise and measurement noise had a standard deviation of 20 mA and 20 mV, respectively. This is a reasonable representation of the uncertainties found in actual applications according to [33], which states that most commercial sensors used in Battery Management Systems lie between 0.1 $\%$ and 1 $\%$ of the measurement range in measurement error. The constant values for the covariance matrices and the inital value for the state-error covariance matrix were then set to

$$\mathbf{\Sigma}_{\tilde{\mathbf{w}}} = \mathbf{Q} = \begin{bmatrix} 0.02^2 & 0 \\ 0 & 0.02^2 \end{bmatrix}, \quad \mathbf{\Sigma}_{\tilde{\mathbf{v}}} = \mathbf{R} = 0.02^2. \tag{5.3}$$

$$\mathbf{\Sigma}_{\tilde{\mathbf{x}},0} = \mathbf{P}_0 = \begin{bmatrix} 0.1 & 0 \\ 0 & 0.1 \end{bmatrix}$$

Simulations of the estimators were then run with 6 cycles of the FUDS as input, with a sampling time of 1s. The ground truth in the simulations for the linear estimators was computed by the Coloumb counting method, i.e. by simulating the SOC state z_k without the addition of simulated measurement noise.

5.7.2 EKF and SPKF

The EKF and SPKF were simulated with the provided MATLAB code from [4] and the UDDS load current profile as input. Here the true initial SOC of the simulated E2 cell was 100 $\%$, and the covariance matrices were set to

$$\boldsymbol{\Sigma}_{\tilde{\mathbf{w}}} = \begin{bmatrix} 0.2 & 0 \\ 0 & 0.2 \end{bmatrix}, \quad \boldsymbol{\Sigma}_{\tilde{\mathbf{v}}} = 0.2. \tag{5.4}$$

$$\boldsymbol{\Sigma}_{\tilde{\mathbf{x}},0} = \begin{bmatrix} 1 & 0 \\ 0 & 1 \end{bmatrix}$$

The applied UDDS load profile had a total of 16 cycles stretched over approximately 11.3 hours, and the simulations were run with a sampling time of 1s. The ambient temperature chosen for the simulation was 5 °C to assess the estimation accuracy for conditions where nonlinear hysteresis is a significant contribution factor to the cell terminal voltage [4]. For these simulations the ground truth was provided by the toolbox.

6

Results

6.1 Linear state estimators

In Figure 6.1 the approximation of the OCV-SOC relationship for the 18650 cell at 25 °C can be observed. The resulting estimated SOC from the simulations using this approximation and the initial tuning of the covariance matrices can be seen in Figure 6.2. In Figure 6.3 the estimation error for the different linear estimators are plotted using the initial tuning. Observe that the 3σ bounds from the LKF are included, which is the bound for which one with 99.7 $\%$ confidence can say that the true state will lay within [4].

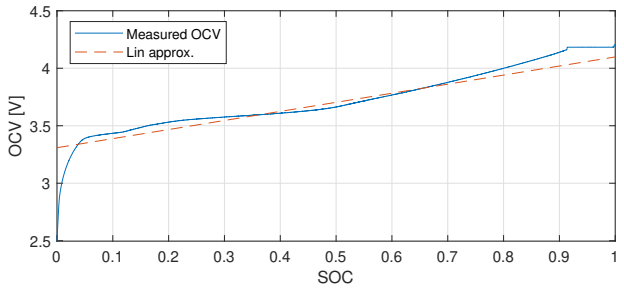

Figure 6.1: Linear approximation of the OCV-SOC relationship for the 18650 cell.

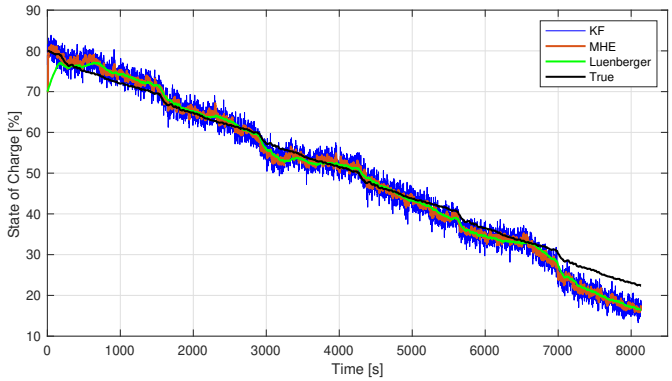

Figure 6.2: Estimated SOC for the three linear state estimators plotted against true SOC for the FUDS cycles.

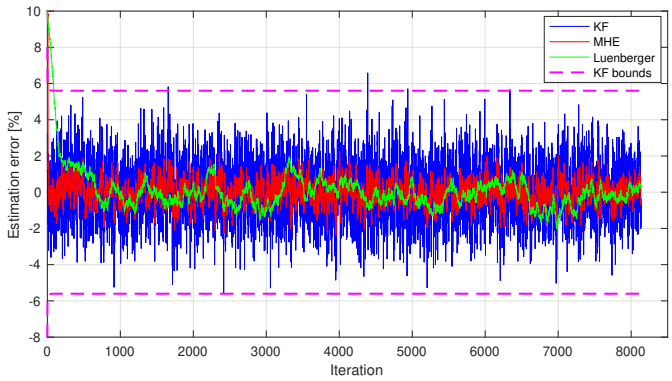

Figure 6.3: Estimation error plotted with the KF 3σ bounds for the FUDS cycles.

Figure 6.4 illustrates the obtained SOC estimates during the FUDS cycles after tuning of the covariance matrices for the KF and MHE, where the corresponding estimation error is plotted in Figure 6.5. Also here the 3σ bounds for the LKF are included in the estimation error plot.

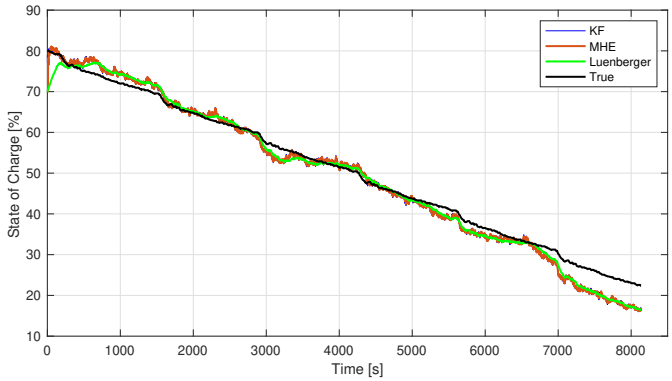

Figure 6.4: Estimated SOC for the three linear state estimators plotted against true SOC for the FUDS cycles after tuning.

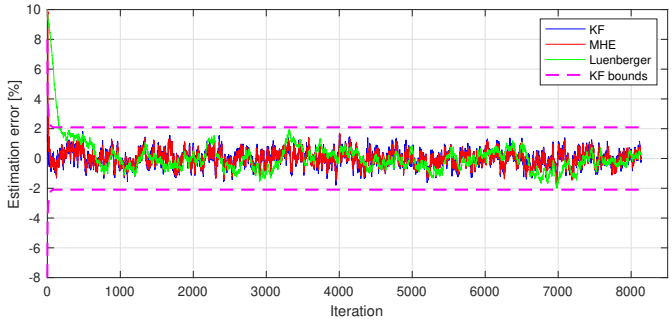

Figure 6.5: Estimation error plotted with the KF 3σ bounds for the FUDS cycles after tuning.

6.2 Nonlinear state estimators

The SOC estimation results acquired from the nonlinear estimators are presented in this section. In Figure 6.6 the SOC estimates produced by the EKF during the UDDS cycles are shown, with the corresponding estimation error plotted in Figure 6.7. The EKF 3σ bounds are included here as well for both plots. In Figure 6.8 the SOC estimates computed by the SPKF during the UDDS cycles can be observed, with the following estimation error and SPKF bounds in Figure 6.9. At the end of the section in Table 6.1 the performance of the SOC estimators are summarized.

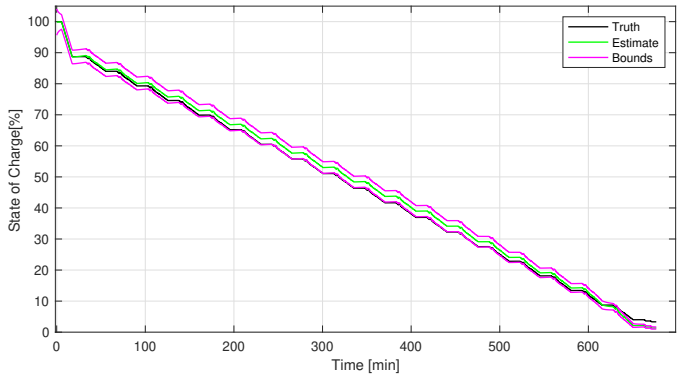

Figure 6.6: EKF estimated SOC plotted against the true SOC with the 3σ bounds.

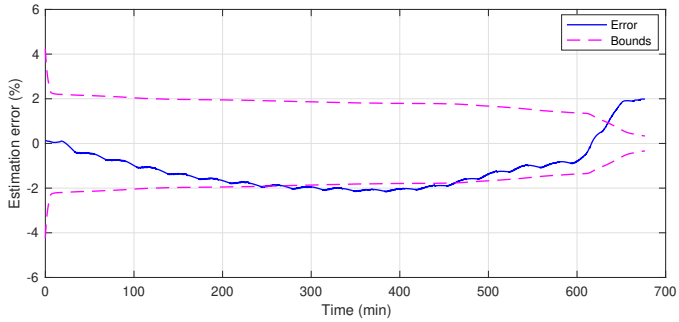

Figure 6.7: EKF SOC estimation error plotted with the EKF 3σ bounds.

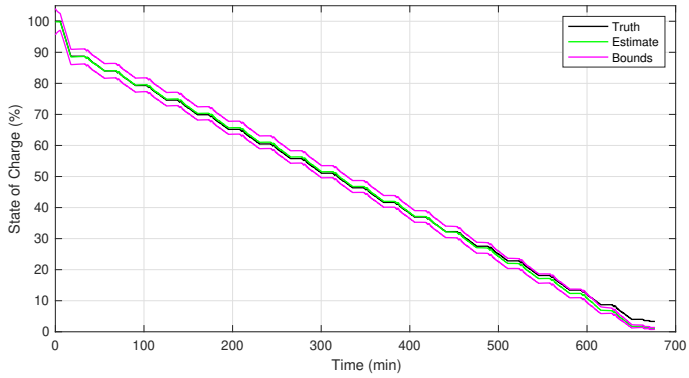

Figure 6.8: SPKF estimated SOC plotted against the true SOC with the 3σ bounds.

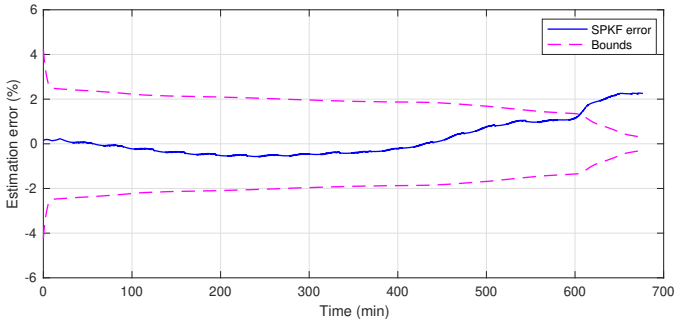

Figure 6.9: SPKF SOC estimation error plotted with the SPKF 3σ bounds.

	RMSE	MAE	Avg. computation time per iteration
Luenberger observer	2.49 %	1.83 %	2.95e-6 s
KF	2.92 %	2.27 %	2.90e-5 s
MHE (N = 10)	2.60 %	1.95 %	9.95e-3 s
KF (tuned)	2.53 %	1.88 %	2.90e-5 s
MHE (N = 10, tuned)	2.53 %	1.88 %	9.95e-3 s
MHE (N = 20, tuned)	2.53 %	1.86 %	10.47e-3 s
MHE (N = 30, tuned)	2.52 %	1.85 %	10.88e-3 s
MHE (N = 100, tuned)	2.52 %	1.81 %	13.35e-3 s
EKF	1.53 %	1.40 %	1.77e-4 s
SPKF	0.84 %	0.61 %	2.51e-4 s

Table 6.1: Summary of performance metrics for the state estimators.

6.3 Single particle model simulation

In Figure 6.10 the lithium-ion surface concentration of an assumed spherical homogeneous electrode particle during the previously specified simulation is observed.

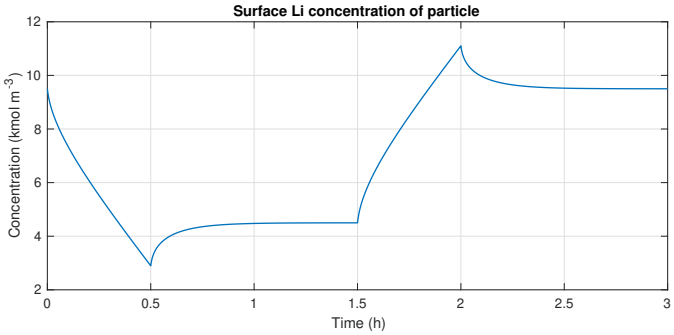

Figure 6.10: The surface concentration of lithium-ions on a spherical electrode particle.

6.4 Battery pack simulation

The results from the battery pack simulations can be observed in this section. Figure 6.11 shows the individual cell currents in each module in a PCM configured battery pack. The resulting indivdual cell SOC in each module are then plotted in Figure 6.12.

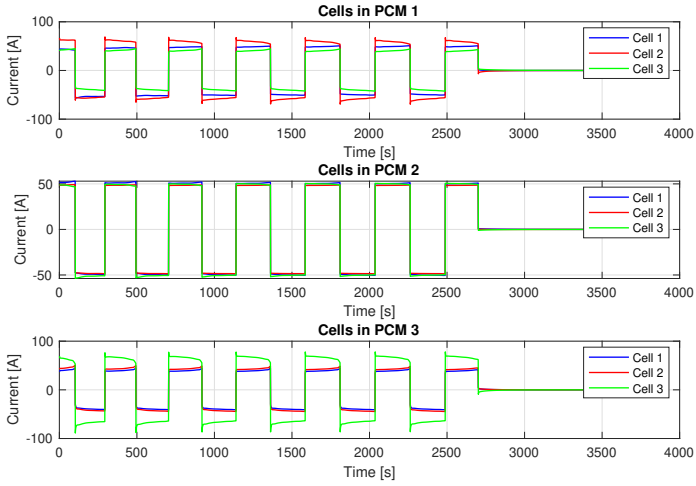

Figure 6.11: The cell currents in each PCM.

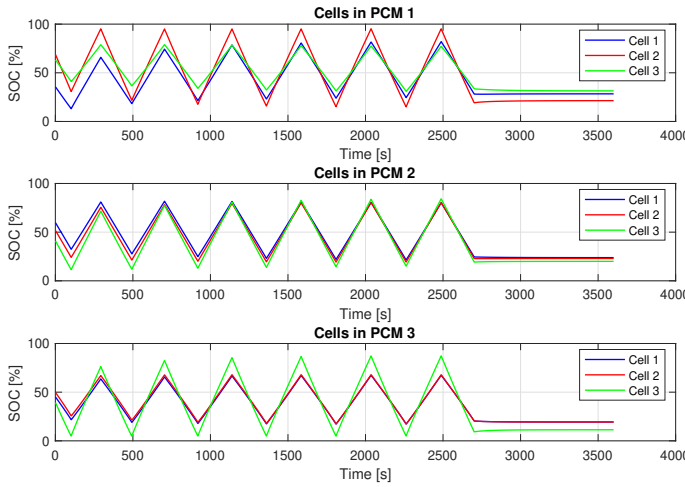

Figure 6.12: The SOC for each cell in each PCM.

6.5 EV simulation

In this section the EV simulation results are presented. From Figure 6.13 the speed and acceleration data of the EV can be seen troughout one cycle of the UDDS. In Figure 6.14 the battery data during the cycle is shown, where the power denotes the delivered power of the battery, and the current is the load current drawn by the electric motor and generated by regenerative breaking [3]. The SOC of the battery pack during the cycle is also plotted.

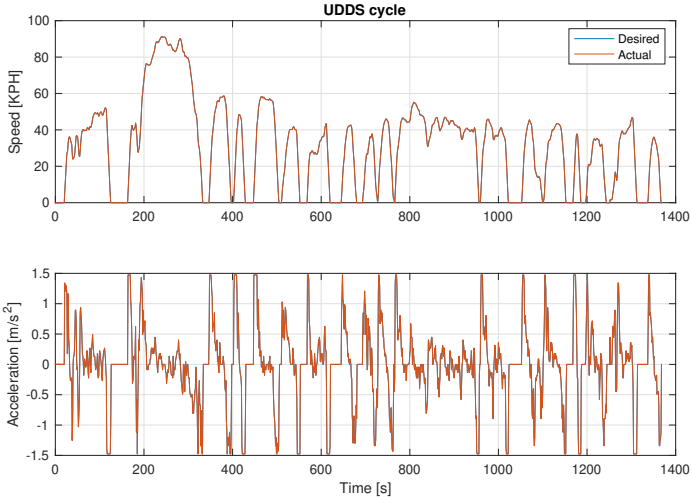

Figure 6.13: The desired and actual speed and acceleration of the EV during one UDDS cycle.

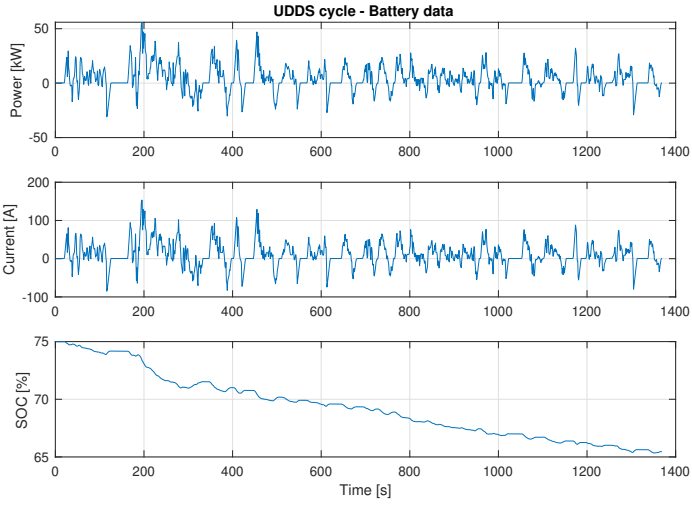

Figure 6.14: The SOC, load current and delivered power of the battery in the EV during one UDDS cycle.

7

Discussion

7.1 Results of SOC estimation

The performance of the linear state estimators were overall reasonably good. They all achieved both a Root-Mean-Square error (RMSE) and a Mean-Absolute error (MAE) in SOC estimation below 3 $\%$ when compared to the true SOC. The Luenberger observer performed very well relative to its simple implementation and function, and actually slightly outperformed both the KF and the MHE in terms of total estimation accuracy, which was surprising. Due to the noisy measurements, it was necessary to place the poles very close to the edge of the unit circle in the complex plane to attenuate noise, which caused a slow convergence of the observer. From Figure 6.2 it can be seen that the Luenberger observer requires about 200s to converge to the proximity of the true SOC, which is much slower than the KF and the MHE. In Table 6.1, the simplicity of the Luenberger observer is reflected in the average required computation time per iteration, which was lowest of all the estimators. Although the performance of all linear state estimators were relatively good when simulated with a constant ambient temperature, they might not suffice for real-world applications where temperature variations are significant and increased estimation error is expected.

When comparing the results in Figure 6.2 and Figure 6.4, it is clear that the KF performed better after tuning, while the performance of the MHE was practically the same after tuning. What is interesting, is the very similar SOC estimation results and trajectory for the KF and the MHE in Figure 6.4. This may be explained by the choice of the arrival cost in the MHE, which is based on Kalman filter state-error covariance updates. Referring to section 4.4 where it was stated that MHE and KF coincide for unconstrained linear systems, it is observed in Figure 6.4 that the inequality constraints are inactive because the SOC lies between 0 and 1 the entire simulation. This is part of the reason for the similar results. However, since the model is included as an equality constraint over the entire

horizon, it would be reasonable to think that more accurate or smoothed estimates could be obtained when compared to the KF. A possible explanation for this is that the model itself as an equality constraint does not provide enough information to improve upon the estimates of the KF. This is possibly verified by the fact an increase in horizon length N for the linear MHE yielded practically the same estimation results except from an increase in computation time. It should be noted here that a faster computation time could have been achieved for the MHE, since the use of a nonlinear solver was unnecessary for the given QP problem. However, a QP solver was not readily available at the time. Based on the performance results, there is no other incentive to use the MHE over the KF for linear systems given the difference in computational cost, other than the fact that the linear MHE can handle system contraints.

The nonlinear estimators performed better in the simulations purely based on the performance metrics in Table 6.1. The SPKF performed best of all the estimators in terms estimation accuracy, yielding an RMS estimation error below 1 $\%$. Although the cell chemistry, the models and the conditions for the simulations of the linear and nonlinear estimators are different, a reasonable comparison can be made. Considering the nonlinear estimators were simulated with an ambient temperature of 5 °C where for instance nonlinear hysteresis is significant, there is reason to believe that a similar ambient temperature would increase the estimation error for the linear estimators, since hysteresis is not included in the linear model. Furthermore, it is clear that the linear approximation of the OCV-SOC curve is simply too inaccurate to able to compete with the more accurate nonlinear OCV-SOC curves of the nonlinear estimators. This is especially true for an SOC below 10 $\%$ and above 90 $\%$, which is evident from Figure 6.1.

Results received from the SPM simulations have provided an understanding of the slow diffusion processes inside lithium-ion batteries. They explain why it can take hours before the diffusion voltages of a battery relaxes entirely, as shown in Figure 6.10. Moreover the simulation has demonstrated the possibilities of using physics-based models for even more accurate, microscale state predictions of internal LIB states. The complexity of these models are however evident from the model derivation and the corresponding simple simulation, which implies that the ECMs provide simpler and more comprehensible battery models.

The additional results obtained from the battery pack simulations have not been discussed in the light of state estimation. They have however highlighted some important aspects to consider when performing state estimation, such as the non-uniqueness in each cell as illustrated in Figure 6.11 and Figure 6.12. Here it is understood that cell-level battery management is important for a BMS, since two equal cells can behave notably different. Moreover, the plots show some of the automatic cell balancing that occur in PCM configured battery packs as the individual cell currents and SOCs converge to the same rest value towards the end of the simulation.

The EV simulations demonstrated their usefulness with the fact that they can simulate the required performance from a battery pack as seen in Figure 6.14. This has not been directly linked with LIB state estimation, but it should be pointed out that before designing battery packs and corresponding LIB state estimators, the dynamics and requirements of the area of application should be simulated and investigated to ensure that there is a good fit between each part. For instance, for slow discharge and charge processes the MHE is better suited than for the faster ones due to extra required computation time. EV simulations can therefore be used to tailor the battery pack and state estimators to the intended area of application, which can be of interest in further work with LIB state estimation.

7.2 Limitations

Limitations of the study conducted in thesis are a few. Ideally, the comparison of linear and nonlinear estimation methods should have been performed on the same battery cell under similar conditions. However, due to the short time span and broad scope of the thesis, this was deemed unrealistic. Therefore pre-identified models were used, and focus was put on learning and laying a good foundation for further work on state estimation for LIBs in the master thesis. Another thing to note is that more, different types of load current profiles should have been applied to the cells at different ambient temperatures to get a broader understanding of the performance of the state estimators, as these conditions are of great significance in state estimation for LIBs.

7.3 Further work

Based on the comparisons presented in this thesis, further work on state estimation for lithium-ion batteries should focus on nonlinear models and estimators. The SPKF demonstrated very accurate SOC estimations even at low ambient temperatures, and should therefore be investigated further. Moreover, despite performing equally well as the Luenberger observer and the KF at a greater computational cost, the MHE should also be studied closer. However, this time it should be implemented with a nonlinar model. The reason for this is that in literature [34] [35], the nonlinear MHE tends to outperform the SPKF/UKF for LIB state estimation. With the addition of system constraint handling as well, improvement on the preservation of the safety and integrity of the battery can be made, which is principal for a BMS.

The CasADi toolbox offers a great framework for implementation and efficient solving of nonlinear optimization problems, and is available for MATLAB, C++ and Python. Another possibility here is to use CasADi in combination with *acados*, which is an open-source software package that provides fast nonlinear optimization solvers for embedded systems as well as an interface to CasADi-written code [36]. An interesting approach would then be to investigate the feasibility of implementing Moving Horizon estimation for the possibly resource-limited systems that are used in a BMS.

Further work should also ideally include more internal states such as SOH and SOAP in the state estimation problem, as these are important to monitor and control in a BMS. The models can potentially also include descriptions of how temperature affects the battery, which could result in even more accurate estimates.

8

Conclusion

The performance evaluation and comparison of the different ECM-based state estimators indicated that the SPKF performed the best with an RMSE and MAE below 1 %. Thereafter the EKF performed well given its non-ideal operating conditions with an RMSE and MAE below 2 %. The linear state estimators all achieved achieved a RMSE and MAE below 3 %, although this was under milder conditions than those of the nonlinear estimators. Here the Luenberger observer performed well relative to its simple implementation and low computational cost. That being said, it is expected that estimation error increases for the linear state estimators with more realistic operating conditions such as low temperatures and temperature variations in general. Therefore further work should focus on using nonlinear models with the SPKF or similar filters and the MHE. In literature, the MHE demonstrated great performance in LIB state estimation with nonlinear models, and should therefore also be studied closer. At last, other important internal states such as SOH and SOAP in the LIB should be included in the state estimation problem to provide a more complete solution.

Bibliography

[1] Reiner Korthauer. *Lithium-Ion Batteries: Basics and Applications*. 2018.

[2] Abbas Fotouhi, Daniel J. Auger, Karsten Propp, Stefano Longo, and Mark Wild. A review on electric vehicle battery modelling: From lithium-ion toward lithium–sulphur. *Renewable and Sustainable Energy Reviews*, 56:1008–1021, 2016.

[3] G. L. Plett. *Battery Management Systems: Volume 1 - Battery Modeling*. Artech House, Massachusetts, United States of America, 2015.

[4] G. L. Plett. *Battery Management Systems: Volume 2 - Equivalent-Circuit Methods*. Artech House, Massachusetts, United States of America, 2016.

[5] Discrete-time luenberger observer, 2017. The Mathworks, Natick, MA, USA.

[6] E.A. Wan and R. Van Der Merwe. The unscented kalman filter for nonlinear estimation. In *Proceedings of the IEEE 2000 Adaptive Systems for Signal Processing, Communications, and Control Symposium (Cat. No.00EX373)*, pages 153–158, 2000.

[7] Fangdan Zheng, Yinjiao Xing, Jiuchun Jiang, Bingxiang Sun, Jonghoon Kim, and Michael Pecht. Influence of different open circuit voltage tests on state of charge online estimation for lithium-ion batteries. *Applied Energy*, 183:513–525, 2016.

[8] Taehoon Kim, Wentao Song, Dae-Yong Son, Luis K. Ono, and Yabing Qi. Lithium-ion batteries: outlook on present, future, and hybridized technologies. *J. Mater. Chem. A*, 7:2942–2964, 2019.

[9] Muhammad Umair Mutarraf, Yajuan Guan, Luona Xu, Chun-Lien Su, Juan C. Vasquez, and Josep M. Guerrero. Electric cars, ships, and their charging infrastructure – a comprehensive review. *Sustainable Energy Technologies and Assessments*, 52:102177, 2022.

[10] Fengchun Sun, Rui Xiong, and Hongwen He. Estimation of state-of-charge and state-of-power capability of lithium-ion battery considering varying health conditions. *Journal of Power Sources*, 259:166–176, 2014.

[11] Yujie Wang, Jiaqiang Tian, Zhendong Sun, Li Wang, Ruilong Xu, Mince Li, and Zonghai Chen. A comprehensive review of battery modeling and state estimation approaches for advanced battery management systems. *Renewable and Sustainable Energy Reviews*, 131:110015, 2020.

[12] Neha Bhushan, Saad Mekhilef, Kok Soon Tey, Mohamed Shaaban, Mehdi Seyedmahmoudian, and Alex Stojcevski. Overview of model- and non-model-based online battery management systems for electric vehicle applications: A comprehensive review of experimental and simulation studies. *Sustainability*, 14(23), 2022.

[13] Prashant Shrivastava, Tey Kok Soon, Mohd Yamani Idna Bin Idris, and Saad Mekhilef. Overview of model-based online state-of-charge estimation using kalman filter family for lithium-ion batteries. *Renewable and Sustainable Energy Reviews*, 113:109233, 2019.

[14] Yuqing Chen, Yuqiong Kang, Yun Zhao, Li Wang, Jilei Liu, Yanxi Li, Zheng Liang, Xiangming He, Xing Li, Naser Tavajohi, and Baohua Li. A review of lithium-ion battery safety concerns: The issues, strategies, and testing standards. *Journal of Energy Chemistry*, 59:83–99, 2021.

[15] Hubert Rubenbauer and Stefan Henninger. Definitions and reference values for battery systems in electrical power grids. *Journal of Energy Storage*, 12:87–107, 2017.

[16] Bizhong Xia, Bo Ye, and Jianwen Cao. Polarization voltage characterization of lithium-ion batteries based on a lumped diffusion model and joint parameter estimation algorithm. *Energies*, 15(3), 2022.

[17] Grzegorz Piłatowicz, Andrea Marongiu, Julia Drillkens, Philipp Sinhuber, and Dirk Uwe Sauer. A critical overview of definitions and determination techniques of the internal resistance using lithium-ion, lead-acid, nickel metal-hydride batteries and electrochemical double-layer capacitors as examples. *Journal of Power Sources*, 296:365–376, 2015.

[18] Jiaqiang Tian, Yujie Wang, and Zonghai Chen. An improved single particle model for lithium-ion batteries based on main stress factor compensation. *Journal of Cleaner Production*, 278:123456, 2021.

[19] Anup Barai, W. Dhammika Widanage, James Marco, Andrew McGordon, and Paul Jennings. A study of the open circuit voltage characterization technique and hysteresis assessment of lithium-ion cells. *Journal of Power Sources*, 295:99–107, 2015.

[20] Federico Baronti, Nicola Femia, Roberto Saletti, Ciro Visone, and Walter Zamboni. Hysteresis modeling in li-ion batteries. *IEEE Transactions on Magnetics*, 50(11):1–4, 2014.

[21] Hongwen He, Rui Xiong, and Jinxin Fan. Evaluation of lithium-ion battery equivalent circuit models for state of charge estimation by an experimental approach. *Energies*, 4(4):582–598, 2011.

[22] Jiahao Li, Joaquin Klee Barillas, Clemens Guenther, and Michael A. Danzer. A comparative study of state of charge estimation algorithms for lifepo4 batteries used in electric vehicles. *Journal of Power Sources*, 230:244–250, 2013.

[23] V. Sundarapandian. A separation theorem for robust pole placement of discrete-time linear control systems with full-order observers. *Mathematical and Computer Modelling*, 43(1):42–48, 2006.

[24] Chi-Tsong Chen. *Linear System Theory and Design*. Oxford University Press, Incorporated, 2014.

[25] *An Evaluation of the Moving Horizon Estimation Algorithm for Online Estimation of Battery State of Charge and State of Health*, volume Volume 4B: Dynamics, Vibration, and Control of *ASME International Mechanical Engineering Congress and Exposition*, 11 2014. V04BT04A049.

[26] Zhongbao Wei, Jian Hu, Yang Li, Hongwen He, Weihan Li, and Dirk Uwe Sauer. Hierarchical soft measurement of load current and state of charge for future smart lithium-ion batteries. *Applied Energy*, 307:118246, 2022.

[27] Christopher V. Rao, James B. Rawlings, and Jay H. Lee. Constrained linear state estimation—a moving horizon approach. *Automatica*, 37(10):1619–1628, 2001.

[28] M. Hovd. A note on the smoothing formulation of moving horizon estimation. *Facta Universitatis. Series: Automatic Control and Robotics*, 11:91–97, 2012.

[29] Gregory L. Plett. Extended kalman filtering for battery management systems of lipb-based hev battery packs: Part 1. background. *Journal of Power Sources*, 134(2):252–261, 2004.

[30] Andreas Manthopoulos and Xiang Wang. A review and comparison of lithium-ion battery soc estimation methods for electric vehicles. In *IECON 2020 The 46th Annual Conference of the IEEE Industrial Electronics Society*, pages 2385–2392, 2020.

[31] Yinjiao Xing, Wei He, Michael Pecht, and Kwok Leung Tsui. State of charge estimation of lithium-ion batteries using the open-circuit voltage at various ambient temperatures. *Applied Energy*, 113:106–115, 2014.

[32] Gillis J. Horn G. et al. Andersson, J.A.E. Casadi: a software framework for nonlinear optimization and optimal control. *Mathematical Programming Computation*, 11:1–36, 2019.

[33] Yuejiu Zheng, Minggao Ouyang, Xuebing Han, Languang Lu, and Jianqiu Li. Investigating the error sources of the online state of charge estimation methods for lithium-ion batteries in electric vehicles. *Journal of Power Sources*, 377:161–188, 2018.

[34] Ji Liu, Sergio Mendoza, and Hosam K. Fathy. Total least squares state of charge estimation for lithium-ion batteries: An efficient moving horizon estimation approach. *IFAC-PapersOnLine*, 50(1):14489–14494, 2017. 20th IFAC World Congress.

[35] A robust approach to state of charge assessment based on moving horizon optimal estimation considering battery system uncertainty and aging condition. *Journal of Cleaner Production*, 270:122508, 2020.

[36] Frison G. Kouzoupis D. et al. Verschueren, R. acados - a modular open-source framework for fast embedded optimal control. *Mathematical Programming Computation*, 14:147–183, 2022.